


# POWER FLOW DYNAMICS AND COUPLING MECHANISMS IN POWER-BY-WIRE ACTUATION: A COMPREHENSIVE MODELING AND ANALYSIS APPROACH

Linlin Jiang[1], Yang Li[2], Shilong Bai[1], Zhuo Li[2], Kaixiang Jia[1] & Yaoxing Shang[1]

[1]School of Automation Science and Electrical Engineering, Beihang University, Beijing 100191, China
[2]National Key Laboratory of Aircraft Integrated Flight Control, Beihang University, Beijing 100191, China

## Abstract

Power-by-wire (PBW) actuation is critical for flight control in more-electric aircraft (MEA). Flight control actuators operating under time-varying conditions induce coupling effects between electric actuators states and electrical power grid states, leading to complex dynamic power flow interactions. These interactions may cause DC-bus voltage fluctuations and even collapse, thereby threatening flight safety. To clarify and quantify the power flow coupling effects,a cross-domain integrated model is developed to reveal how flight-control information flow is transformed into actuation–electrical-grid energy flow, with key cross-domain parameters calculated for system-level dynamic coupling characterization of the flight-control, actuation, and electrical power subsystems. A real-time simulation platform was developed to implement and validate the proposed cross-domain integrated dynamic model. Based on the proposed model, a time–frequency-domain principal-component power spectrum analysis method is developed to extract the dominant Electro-hydrostatic actuator (EHA) power-demand spectra under different flight missions, providing representative load profiles for EHA ground testing and design without relying on real flight tests. Moreover,the resulting power-flow data are further analyzed to characterize both single-EHA–grid and multi-EHA–grid coupling features.A dedicated experimental platform is constructed to validate the identified single- and multi-EHA power-flow coupling characteristics, and a 92.4% agreement in single-EHA–grid power-flow validation confirms the rationality and effectiveness of the proposed comprehensive modeling and analysis approach.The proposed approach provides support for the optimized design of aircraft electrical power, flight control, and actuation systems in MEA.

**Keywords:** More-electric aircraft (MEA);Power-by-wire(PBW) actuation;Electro-hydrostatic actuator (EHA);Energy regeneration;Power flow analysis

## 1. Introduction

Recently, aircraft electrification has rapidly advanced due to demands for environmental protection, fuel economy, and operational cost optimization. More-electric aircraft (MEA) have become critical directions in aviation development [1, 2]. Flight control systems in MEA adopt power-by-wire(PBW) actuation schemes [3, 4]. Electrical energy is transmitted via cables to drive electric actuators locally, which deflect control surfaces for reliable flight operations. This approach has been implemented in primary and secondary flight control surfaces of MEA such as the A350 and F-35 [5, 6].

Electric actuators operate in four-quadrant modes based on the flight state. When the direction of actuator speed is aligned with direction of output force, it acts as a drive source, consuming energy. Conversely, when the speed opposes the force direction, external aerodynamic loads drive the actuator, enabling energy regeneration [7]. During actual operation, each electric actuator frequently starts and stops in response to the changing of flight state, and the motors of actuators alternate between operating as reverse-load motors and forward-load generators, thereby creating a complex and dynamic power flow relationship that couples with the operational state of the electrical power

https://doi.org/10.71945/icas2026_0561

grid. Such uncertain power flow interactions impact grid stability, and may even triggering DC bus voltage collapse under severe conditions, and threatening flight safety.

Existing studies on power characteristics of electric actuator and the power flow coupling with aircraft electrical power grids can generally be categorized into two main streams. One stream focuses on acquiring realistic power profiles, such as full-envelope flight testing [8], while the other emphasizes rated-condition simulations and model-based extrapolation. Flight tests are capable of capturing realistic actuator power profiles; however, they are costly and provide limited insight into transferable physical mechanisms.

Simulations based on rated conditions or prescribed load spectra facilitate qualitative analysis but fail to adequately represent the real-time control commands and aerodynamic-load-driven power flow interact characteristics during actual flight missions [9, 10]. Independent modeling of the power grid and electric actuators is valuable for investigating power flow interaction characteristics. However, existing studies are largely confined to either the power grid or the electric actuators themselves, while the other subsystem is treated in a simplified manner [11, 12, 13]. As a result, a fully unified system-level perspective has not yet been sufficiently established, which limits the ability to elucidate the mechanisms of power flow interactions and to quantitatively assess the combined effects of multiple electric actuators on the stability of the aircraft electrical power system.

To address these challenges, this paper develops a cross-domain dynamic integrated modeling and analysis approach for the flight control–actuation–electrical power grid system. The approach supports mission-dependent EHA power-spectrum extraction without relying on real flight tests and enables quantitative characterization of coupling power-flow propagation across single- and multi-actuator configurations.

The remainder of this paper is organized as follows. Section 2 establishes a cross-domain dynamic integrated model for the flight-control–actuation–power-grid system, where information-domain and energy-domain variables are quantitatively linked through key cross-domain parameters. A real-time simulation platform is further developed to implement and validate the proposed model. Section 3 proposes the actuator power-spectrum analysis and power-flow coupling characteristic analysis methods for extracting mission-dependent EHA power spectra and characterizing single- and multi-actuator coupling features. Section 4 presents the power-flow characteristic test bench and validates the model accuracy and analysis effectiveness through simulation–experiment comparisons under typical flight missions. Finally, Section 5 concludes the paper by summarizing the main findings.

## 2. Modeling and Simulation

To accurately predict power coupling relationships between multiple electric actuators and the electrical power grid under varying maneuvers, a cross-domain dynamic integrated model is established. As shown in Figure 1, this model characterizes the dynamic transfer mechanisms between flight missions and power flow interactions within the information-domain and energy domain. Parameters in the information domain, such as target control surface deflection $\delta_{ref}$and hinge moments$M_h$, are input into the energy domain. Conversely, parameters in the energy domain, such as actuator displacements $X_p$ and measured control surface deflection angles $\delta$ are fed back into the information domain. Critical parameters, including target control surface deflection angles and hinge moments, are solved to determine real-time actuator power demands, which critically influence power coupling dynamics. The following sections detail the real-time solving methods for critical interactive parameters, power flow mechanisms, and features of the real-time simulation platform.

### 2.1 Information-domain Modeling

To accurately obtain critical flight control system parameters,witch related to actuator energy characteristics (e.g., the target control surface deflection angles and hinge moments), Based on the Flight Control System architectures [14, 15], this study proposes a mission-oriented real-time computing method for flight control commands and aerodynamic loads. A closed-loop automatic flight control system model is developed, focusing on information-domain modeling within the cross-domain integrated framework.

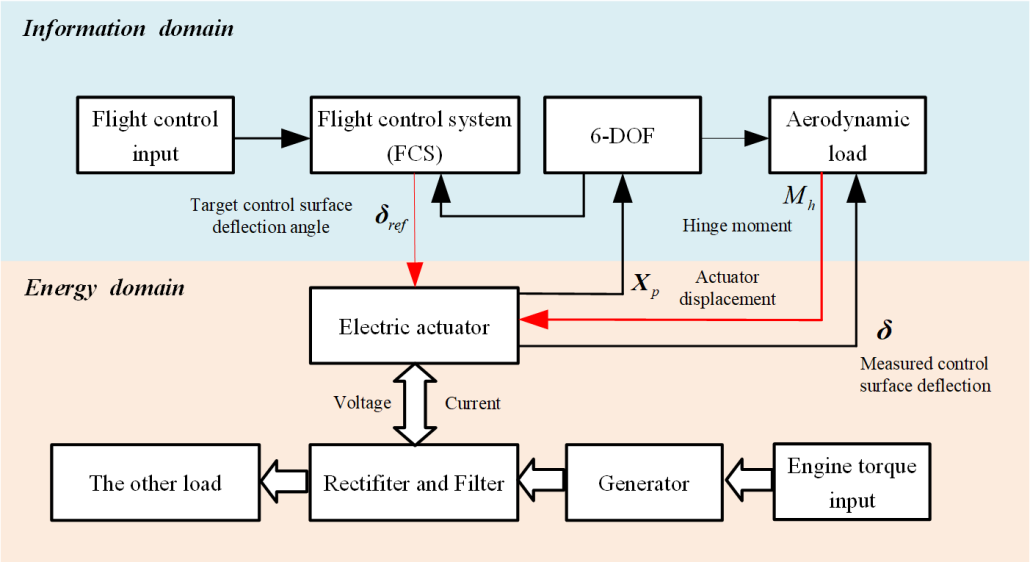



Figure 1 – The structure of cross-domain dynamic integrated model.

### 2.1.1 Flight State Analysis

Accurate flight mission decomposition and state analysis form the basis for hinge moment calculations. Twelve critical flight state parameters related to aerodynamic loads are selected.(Table 1)

Table 1 – Critical flight state parameters

| Parameter | Symbol | Unit |
|---|---|---|
| Speed | V | m/s |
| Aircraft angle of attack | $\alpha$ | rad |
| Aircraft angle of sideslip | $\beta$ | rad |
| Euler angles | $\phi, \theta, \psi$ | rad |
| Body-fixed angular rates | $p, q, r$ | \$rad/s |
| Earth-fixed coordinate | $x_g, y_g$ | |
| Altitude | h | m |

Based on aircraft kinematics, the differential forms of angular velocities about the body-fixed axes were derived.

$$\begin{cases} \dot{p} = (c_1 r + c_2 p)q + c_3 \bar{L} + c_4 N \\ \dot{q} = c_5 pr + c_6 (p^2 - r^2) - c_7 M \\ \dot{r} = (c_8 p - c_2 r)q + c_4 \bar{L} + c_9 N \end{cases} \tag{1}$$

where $\bar{L}$is the rolling moment, M is the pitching moment, and N is the yawing moment.The coefficients $c_1 \sim c_9$ were defined as follows:

$$\begin{cases} c_1 = \frac{(I_y - I_z)I_z - I_x^2}{I_x I_z - I_x^2} \\ c_2 = \frac{(I_x - I_x + I_z)I_x}{I_x I_z - I_x^2} \\ c_3 = \frac{I_x}{I_x I_z - I_x^2} \\ c_4 = \frac{I_x}{I_x I_z - I_x^2} \\ c_5 = \frac{I_z - I_x}{I_y} \\ c_6 = \frac{I_x}{I_y} \\ c_7 = \frac{1}{I_y} \\ c_8 = \frac{I_x(I_x - I_y) + I_x^2}{I_x I_z - I_x^2} \\ c_9 = \frac{I_x}{I_x I_z - I_x^2} \end{cases} \tag{2}$$

where $I_x, I_y, I_z$ are the moments of inertia about the body-fixed $x_b, y_b$, and $z_b$ axes, respectively. $I_{xz}$ is the product of inertia about the $Ox_{\mathrm{b}}z_{\mathrm{b}}$.
Additionally, the resultant external forces in the body-fixed coordinate system, including gravity and thrust components, were combined with aerodynamic forces. The differential forms of aircraft translational velocities along the three body-fixed axes were expressed as follows:

$$\begin{cases} \dot{u} = vr - wq - g\sin\theta + \frac{F_x}{m} \\ \dot{v} = -ur + wp + g\sin\phi\cos\theta + \frac{F_y}{m} \\ \dot{w} = uq - vp + g\cos\phi\cos\theta + \frac{F_z}{m} \end{cases} \tag{3}$$

where $u, v, w$ are the three-axis velocities; $F_x$, $F_y$, and $F_z$ are the resultant external forces (excluding gravity) along$x_b, y_b$ and $z_b$ axes. $m$ is the aircraft mass, and $g$ is the gravitational acceleration. The current air speed $V$, angle of attack $\alpha$ , and sideslip angle $\beta$ are derived as follows:

$$V = \sqrt{u^2 + v^2 + w^2} \tag{4}$$

$$\begin{cases} \cos\alpha\cos\beta = u/V \\ \sin\beta = v/V \\ \sin\alpha\cos\beta = w/V \end{cases} \tag{5}$$

Using rotational and translational kinematics, the aircraft's attitude angles at the current time step were solved. These results were fed back into aero-dynamic calculations for the next time step.
Equations 1-5 form a closed nonlinear differential system $E\dot{x} = Ax_s + B\delta_{ref}$, establishing a nonlinear differential function relationship between the target control surface deflection angle input vector and the twelve dimensional flight state vectors. With known aircraft parameters, control surface commands, and prior flight states, the aircraft's flight state at any subsequent time can be dynamically solved. In addition, the flight dynamics and aerodynamic models were established based on references [14], which are not elaborated here.

### *2.1.2 Flight Controller Design*

In specific mission scenarios, the target flight state parameters of the aircraft $\mathbf{x}_{ref}$ are generated either by the pilot or the autopilot. The flight control computer then calculates the desired target control surface deflection angles $\delta_{ref}$.The dynamic gain and bandwidth of the flight control law influence the target control surface deflection angle.
By selecting the equilibrium point, the six degree-of-freedom nonlinear differential equations of the aircraft were expanded near the reference point using a Taylor series expansion. The conditions for this reference motion were defined.

$$\beta = \phi = p = q = r = 0 \dot{V} = \dot{\alpha} = \dot{\beta} = \dot{p} = \dot{q} = \dot{r} = 0 \tag{6}$$

The nonlinear state equation set is decomposed into linearized small perturbation motion equations for longitudinal motion (within the $Ox_{\mathrm{b}}z_{\mathrm{b}}$ plane of the body-fixed coordinate system) and lateral-directional motion (within the $Ox_{\mathrm{b}}z_{\mathrm{b}}$ plane of the body-fixed coordinate system). These linearized equations for both longitudinal and lateral-directional small perturbation motions were formulated as linear state equations $\mathbf{E\dot{x}} = \mathbf{Ax} + \mathbf{Bu}$ .The characteristic determinant for longitudinal motion can be expressed as follows:

$$\Delta_L = |s\mathbf{E} - \mathbf{A}| = \begin{vmatrix} s - (X_V + X_{T_V}\cos\alpha_{\mathrm{e}}) & -X_\alpha & g\cos\mu_{\mathrm{e}} & 0 \\ -(Z_V - X_{T_V}\sin\alpha_{\mathrm{e}}) & (V - Z_{\dot{\alpha}})s - Z_\alpha & g\sin\mu_{\mathrm{e}} & -(V + Z_q) \\ 0 & 0 & s & -1 \\ -(M_V + M_{T_V}) & -(M_{\dot{\alpha}} + M_\alpha) & 0 & s - M_q \end{vmatrix} \tag{7}$$

The characteristic equation $\Delta_L = 0$ for longitudinal motion consists of two quadratic factors, representing the long-period and short-period modes, respectively. The long-period mode corresponds to a pair of relatively small complex conjugate roots, characterized by a long oscillation period and slow decay, which reflects the force rebalancing process. $\Delta V(t)$ and $\Delta\theta(t)$ are the state variables associated with the long-period mode. In contrast, the short-period mode corresponds to a pair of

relatively large complex conjugate roots, characterized by a short oscillation period and rapid decay, representing the moment rebalancing process. $\Delta\alpha(t)$ and $\Delta q(t)$ are the state variables associated with the short-period mode. The characteristic determinant for lateral-directional motion is given as follows:

$$\Delta_{LD} = |s\mathrm{E} - \mathbf{A}| = \begin{vmatrix} s - \frac{Y_\beta}{V} & \frac{-g\cos\mu_\mathrm{e}}{V} & \frac{-Y_p}{V} & \frac{-(Y_r - V)}{V} \\ 0 & s & \frac{-\cos\mu_\mathrm{e}}{\cos\theta_\mathrm{e}} & \frac{-\sin\mu_\mathrm{e}}{\cos\theta_\mathrm{e}} \\ -L_\beta^* & 0 & s - L_p^* & -L_r^* \\ -N_\beta^* & 0 & -N_p^* & s - N_r^* \end{vmatrix} \tag{8}$$

By ignoring the gravity terms in Equation 8 and expanding along the second column, and since the values of $Y_p, Y_r, N_p^*$ are relatively small, the characteristic equation is simplified:

$$\Delta_{LD} = \mid sI - A \mid = s\left(s - L_p^*\right)\left[s^2 - s\left(N_r^* + \frac{Y_\beta}{V}\right) + \left(N_\beta^* + \frac{Y_\beta N_r^*}{V}\right)\right] \tag{9}$$

Equation 9 shows that the lateral-directional motion has a real zero root close to the spiral pole and roots near the roll damping points, while the quadratic roots correspond to the Dutch roll poles.
Considering the actual measurement accuracy of the navigation and positioning systems and the requirements of the flight controller, the feedback state varia-bles were selected, combining both longitudinal and lateral-directional motions to form a complete state-space representation of the six-degree-of-freedom aircraft motion.

$$\begin{cases} \dot{\mathbf{x}} = \mathbf{A}\mathbf{x} + \mathbf{B}\mathbf{u}_\mathbf{cmd} \\ \mathbf{y} = \mathbf{C}\mathbf{x} + \mathbf{D}\mathbf{u}_\mathbf{cmd} \end{cases} \tag{10}$$

where$\mathbf{y} = [N_z, q, \alpha, \theta, V, N_y, p, r, \beta, \phi]^\mathrm{T}$is the load factor of axis, $N_z = \frac{F_z}{mg}$ is the load factor of $z_\mathrm{b}$ axis. Assuming the command input vector $\mathbf{u}_{cmd}$ and the flight state vector $x$ is linearly related through negative feedback.

$$\mathbf{u}_\mathbf{cmd} = -\mathbf{k}\mathbf{x} \tag{11}$$

The state-space expression is rewritten as follows:

$$E\dot{x} = Ax + Bu_{cmd} = (A - Bk)x = A_{cl}x \tag{12}$$

The eigenvalues of the closed-loop state-space matrix $A_{cl}$ determine the target control surface deflection angle $\delta_{ref}$.
The input feedback matrix $\mathbf{k}$ is determined using the LQR control method, which in turn determines the closed-loop state-space matrix $A_{cl}$ . The cost function is shown as follows:

$$J = \int \left(x^\mathrm{T} Q x + u_\mathrm{cmd}^\mathrm{T} R u_\mathrm{cmd}\right) \mathrm{d}t \tag{13}$$

In Equation 13, both $\mathbf{Q}$ and $\mathbf{R}$ are diagonal matrices, ensuring that the objective function is a positive definite quadratic form. The larger the value of $\mathbf{Q}$ , the greater the influence of the flight state vector$\mathbf{x}$ ; similarly, the larger the value of $\mathbf{R}$, the greater the influence of the control input command $\mathbf{u}_\mathbf{cmd}$ .By predefining $\mathbf{Q}$ and $\mathbf{R}$ ,the feedback matrix $\mathbf{k}$ is optimized to minimize the objective function $J$ while maintaining system stability.
It is important to note that in longitudinal motion, only the convergence process of the short-period mode state variables is considered. The state vector is $\mathbf{x}=[\alpha, q, N_z]^T$,the input vector is $\mathbf{u}_\mathbf{cmd} = [\delta_\mathrm{t}, \delta_\mathrm{e}]^\mathrm{T}$. In lateral-directional motion, only the convergence pro-cess of the Dutch roll mode state variables is considered. The state vector is $\mathbf{x}=[\beta, p, r, p_s, N_y + r]^T$ and the input vector is $\mathbf{u}_\mathbf{cmd} = [\delta_\mathrm{a}, \delta_\mathrm{r}]^\mathrm{T}$, including the steady roll rate , as shown in Figure 2.

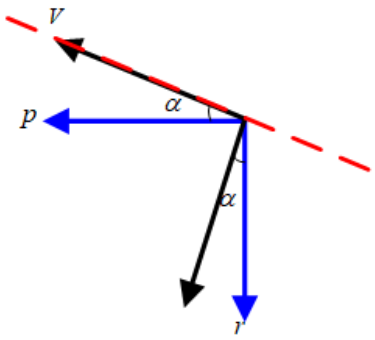



Figure 2 – The Schematic diagram of steady-state roll rate.

### 2.1.3 The hinge moment calculation

The hinge moment represents the aerodynamic torque exerted on the control surface about its hinge axis and can be expressed as follows:

$$M_h = C_{\mathrm{h}} Q_{\mathrm{cs}} S_{\mathrm{w}} c_{\mathrm{A}} \tag{14}$$

where $C_{\mathrm{h}}$ is the hinge moment coefficient, defined as:

$$C_{\mathrm{h}} = C_{\mathrm{h0}} + C_{\mathrm{h},\alpha}\left(Ma\right)\alpha_{\mathrm{eff}} + C_{\mathrm{h},\delta}\left(Ma,\delta\right)\delta \tag{15}$$

where $C_{\mathrm{h0}}$ is the hinge moment coefficient at zero angle of attack, zero control surface deflection, and zero trim tab deflection, generally assumed to be zero. $C_{\mathrm{h},\alpha}\left(Ma\right)$ is the derivative of the hinge moment coefficient with respect to the local airflow incidence angle at the hinge line centre, and is the derivative with respect to the control surface deflection $\delta$ .$Q_{\mathrm{cs}}$ represents the local dynamic pressure at the hinge line centre [16].

The hinge moment is defined as positive when it forces the control surface to deflect in the commanded direction, opposite to the aerodynamic moment convention. Both $C_{\mathrm{h},\alpha}\left(Ma\right)$ and $C_{\mathrm{h},\delta}\left(Ma,\delta\right)$ are negative.

During actual flight, aircraft motions such as sideslip, yaw, and roll prevent the use of aircraft airspeed as the local velocity at the control surface. The local translational velocities at the control surface along the body-fixed , $x_{\mathrm{b}}, y_{\mathrm{b}} z_{\mathrm{b}}$ axes are denoted as $u_{cs}, v_{cs}, w_{cs}$, respectively. Thus, $Q_{\mathrm{cs}}$ can be calculated as follows:

$$Q_{\mathrm{cs}} = \frac{1}{2}\rho\left(u_{\mathrm{cs}}^2 + v_{\mathrm{cs}}^2 + w_{\mathrm{cs}}^2\right) \tag{16}$$

The local airflow incidence angle $\alpha_{\mathrm{eff}}$ is derived as:

$$\alpha_{\mathrm{eff}} = \alpha_{\mathrm{s}} + \tan^{-1}\left(\frac{\varsigma_{\mathrm{cs}}}{u_{\mathrm{cs}}}\right) \tag{17}$$

where $\alpha_{\mathrm{s}}$ is the installation angle of the control surface. For ailerons, elevators, flaperons, and horizontal stabilizers, $\varsigma_{\mathrm{cs}} = w_{\mathrm{cs}}$ ; for the rudder,$\varsigma_{\mathrm{cs}} = v_{\mathrm{cs}}$.

The local translational velocities at the hinge line center are calculated by considering the angular velocity offset between the control surface hinge axis and the aircraft center of mass. Taking the right aileron as an example, the local translational velocity at its hinge line center is expressed as:

$$\begin{cases} u_{\mathrm{cs}} = u - r\Delta y_{\mathrm{a}} + q\Delta z_{\mathrm{a}} \\ v_{\mathrm{cs}} = v - r\Delta x_{\mathrm{a}} - p\Delta z_{\mathrm{a}} \\ w_{\mathrm{cs}} = w + q\Delta x_{\mathrm{a}} + p\Delta y_{\mathrm{a}} \end{cases} \tag{18}$$

Similarly, the left aileron's velocity is given as:

$$\begin{cases} u_{\mathrm{cs}} = u + r\Delta y_{\mathrm{a}} + q\Delta z_{\mathrm{a}} \\ v_{\mathrm{cs}} = v - r\Delta x_{\mathrm{a}} - p\Delta z_{\mathrm{a}} \\ w_{\mathrm{cs}} = w + q\Delta x_{\mathrm{a}} - p\Delta y_{\mathrm{a}} \end{cases} \tag{19}$$

where $\Delta x_{\mathrm{a}}, \Delta y_{\mathrm{a}}, \Delta z_{\mathrm{a}}$ represent the positional offsets between the left/right ailerons and the aircraft center of mass in the body-fixed coordinate system, assuming symmetric aileron configurations. This methodology also applies to elevator and the rudder.
The Information-domain part of the cross-domain dynamic integrated model can be summarized with the following main features:

- Starting from the flight mission, an automatic flight control system model capable of closed-loop control functions is established.
- The influence of flight control laws on the maneuver deflection curve and target deflection angles is considered.
- A non-linear mapping relationship between flight state vectors related to hinge moment calculation is established.
- The effects of local translational velocity of the control surface and local airflow incidence angle on the hinge moment were considered.

## 2.2 Energy-domain Modeling

An important feature of the cross-domain dynamic integrated model is its ability to describe the electromechanical-hydraulic energy conversion and transfer mechanisms within the PBW and the electrical power grid of aircraft system. This section focuses on modeling the energy domain of the cross-domain dynamic integrated model and explicating the hidden energy characteristics in the transfer pathways. As an example, the electro-hydrostatic actuator (EHA), which has a relatively complex structure, is selected to illustrate the application of electric actuators.

### *2.2.1 Electrical Grid Model*

The energy source of the aircraft electrical grid originates from the shaft power of the engine.The MEA typically employ a three-stage aircraft generator that outputs three-phase alternating current. The three-phase AC is converted into 270 VDC through transformer-rectifier units (TRUs), and then collected on the high-voltage DC bus to supply power to onboard loads [17, 18]. In particular, a filter capacitor is connected in parallel between the TRU and the DC bus to smooth the rectified high-voltage DC output and maintain the power quality of the DC bus.
The modeling of the three-stage generator for aviation is based on the Park transformation, yielding the fundamental equations of the main generator, AC main exciter, and permanent magnet auxiliary exciter in the $dq0$ coordinate system.
Main generator voltage equation

$$\begin{cases} u_{dm} = -r_a i_d + p\psi_d - \omega_r \psi_q \\ u_q = -r_a i_q + p\psi_q + \omega_r \psi_d \\ u_0 = -r_a i_0 + p\psi_0 \\ u_f = r_f i_f + p\psi_f \\ u_D = r_D i_D + p\psi_D = 0 \\ u_Q = r_Q i_Q + p\psi_Q = 0 \end{cases} \tag{20}$$

where $\omega_r$ is the rotor electrical angular speed, and $r_a, r_f, r_D, r_Q$ are the resistances of the armature, field, d-axis damping, and q-axis damping windings, respectively.
Main generator flux linkage equation

$$\begin{cases} \psi_d = -L_d i_d + M_{af0} i_f + M_{aD0} i_D \\ \psi_q = -L_q i_q + M_{aQ0} i_Q \\ \psi_0 = -L_0 i_0 \\ \psi_f = -\frac{3}{2} M_{af0} i_d + L_{ff} i_f + M_{fD} i_D \\ \psi_D = -\frac{3}{2} M_{aD0} i_d + M_{Df} i_f + L_{DD} i_D \\ \psi_Q = -\frac{3}{2} M_{aQ0} i_q + L_{QQ} i_Q \end{cases} \tag{21}$$

where $L_{ff}$ is the self-inductance of the field winding, $L_{DD}$ is the self-inductance of the d-axis damping winding, and $L_{QQ}$ is the self-inductance of the q-axis damping winding. $L_d$ and $L_q$ are the d-axis and q-axis synchronous inductances, and $L_0$ is the zero-sequence inductance.
The AC exciter in the three-stage generator is a rotating armature-type synchronous generator. Unlike the main generator, it does not have damping windings. Its voltage, flux, and torque equations are similar and were not detailed [19, 20].
The permanent magnet auxiliary exciter in the three-stage generator uses permanent magnets for excitation. Its voltage equation

$$\begin{cases} u_{dp} = R_s i_{dp} + L_{dp} p i_{dp} - \psi_{qp} \omega_e \\ u_{qp} = R_s i_{qp} + L_{qp} p i_{qp} - \psi_{dp} \omega_e \\ u_{0p} = R_s i_{0p} + L_{0p} p i_{0p} \end{cases} \tag{22}$$

where $R_s$ is the stator winding resistance, and $L_{dp}$,$L_{qp}$,$L_{0p}$ are the synchronous inductances of the d-axis, q-axis, and zero-sequence, respectively.
Permanent magnet synchronous exciter flux linkage equation

$$\begin{cases} \psi_{dp} = L_{dp} i_{dp} + \psi_m \\ \psi_{qp} = L_{qp} i_{qp} \\ \psi_{0p} = L_{0p} i_{0p} \end{cases} \tag{23}$$

where $\psi_m$ is the flux linkage of the fundamental wave of the permanent magnet excitation through the stator winding.
From Equation 20-Equation 23, it can be seen that the energy transfer relationship between the engine speed input and the dq-axis voltage/current of the aviation three-stage AC generator is established. The three-phase uncontrolled rectifier with a filter capacitor converts the three-phase AC generated by the aviation three-stage generator into 270VDC, supplying power to the high-voltage DC bus for electric actuators and other loads.
The TRU typically consists of transformer cascaded with a multi-pulse diode rectifier bridge. The diode bridge rectifier constitutes the core energy conversion stage of the TRU. In this study, a three-phase uncontrolled bridge rectifier is considered, and its dynamics are represented using a controlled-source equivalent model.
Under continuous commutation conditions, the TRU output voltage, which corresponds to the DC bus voltage, can be expressed as

$$\begin{cases} u_d = \frac{1}{k_u} \cdot U_{bus} \sin(\arctan \frac{I_q}{I_d} - \phi) \\ u_q = \frac{1}{k_u} \cdot U_{bus} \cos(\arctan \frac{I_q}{I_d} - \phi) \\ i_{bus} = k_i \cdot \sqrt{i_d^2 + i_q^2} \end{cases} \tag{24}$$

where the voltage regulation parameter $k_u$, current regulation parameter $k_i$ , and phase lag angle $\phi$ can be obtained from switching-model simulations at different steady-state operating points of the system [21].
Based on the current balance at the DC bus node, the rectifier output current satisfies

$$i_{bus} = C_{dc} \cdot \dot{U}_{bus} + i_{RL} + i_{EHA} \tag{25}$$

where $C_{dc}$ denotes the DC-bus capacitance, $i_{RL}$ represents the aggregated loads current excluding the EHA, and $i_{EHA}$ is the EHA current.

### 2.2.2 EHA Energy Model

EHA is a highly integrated local electro-hydraulic hybrid actuator [22, 23, 24]. It consists of a motor, pump, hydraulic cylinder, and tank, forming a volume control system. The system structure is shown in Figure 3. In the PBW actuation, each electric actuator is connected to the electrical power grid as an electrical load, sharing the electrical energy provided by the electrical grid. The real-time power demand of the electric actuator is the active factor that determines the dynamic power flow relationship between the actuator and the electrical power grid of aircraft system.

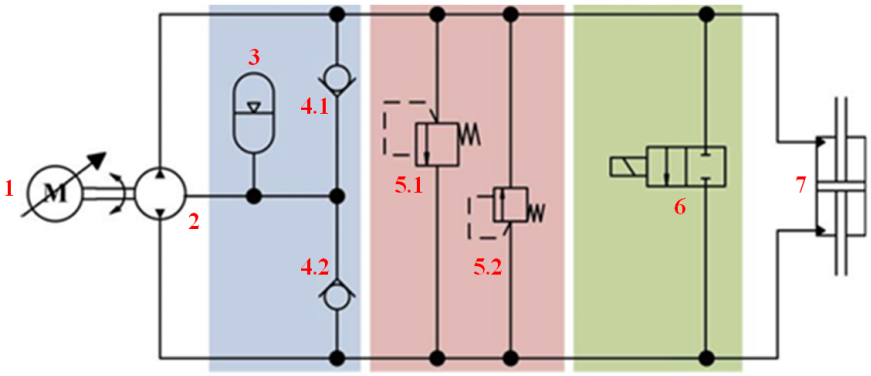



Figure 3 – The schematic diagram of EHA.

The dynamic force balance of the EHA can be expressed as

$$A_p \cdot \Delta P(t) = m_t \ddot{x}_p(t) + c_m \dot{x}(t) + F_L(t) \tag{26}$$

where $m_t$ denotes the total translating mass of the piston and piston rod, $c_m$ is the equivalent damping coefficient, $\Delta P$ is the effective piston area, and is the system pressure differential. $\Delta P$ indicates that, during energy transmission, the mechanical energy required to overcome the aerodynamic load is converted into hydraulic energy within the local closed-loop hydraulic system.
The flow continuity equation of the electro-hydrostatic actuator is given by

$$k_d \cdot D_p \cdot \omega(t) = A_p \dot{x}_p(t) + \frac{V_l}{\beta_e} \Delta \dot{P}(t) + C_A \cdot \Delta P(t) \tag{27}$$

where $D_p$ is the pump displacement, $\omega$ is the pump speed, $V_l$ is the total control volume between the pump and the cylinder, $\beta_e$ is the effective bulk modulus of the hydraulic oil, and $C_A$ is the internal leakage coefficient. The variable $\omega$ reflects that, during energy transmission, the hydraulic energy demanded by the closed hydraulic loop formed by the pump and the cylinder is converted into mechanical energy on the motor-pump shaft. If the hydraulic pump is directly connected to the motor shaft without a speed reducer, the motor speed equals the pump speed. The torque dynamics of the motor can then be written as

$$K_t \cdot i_{EHA}(t) = J\dot{\omega}(t) + k_f \omega(t) + D_p \cdot \Delta P(t) \tag{28}$$

where $J$ is the total equivalent rotational inertia on the motor shaft, $k_f$ is the viscous damping coefficient referred to the motor armature, $K_t$ is the torque constant, and $i$ is the EHA motor current. The variable $i$ shows that, during energy transmission, the mechanical energy demand on the motor and shaft is further converted into electrical energy demand. The voltage dynamic equation of the motor is given by

$$U_c(t) = K_e \omega(t) + L\frac{di_{EHA}(t)}{dt} + Ri_{EHA}(t) \tag{29}$$

where $K_e$ is the back electromotive force constant, $U_c$ is the EHA motor control voltage, $R$ is the total armature resistance, and $L$ is the armature inductance.

## 2.3 Real-time Simulation

The real-time simulation platform is developed by linking the outputs of MATLAB/Simulink with the developed AMEsim environment. This platform enables dynamic power flow interactions analysis and visualization for the PBW actuation system. The information domain of the cross-domain integrated model operates in the M&S environment, while the energy domain runs in AMEsim. MATLAB's numerical computation capabilities and AMEsim's power bond graph modeling are fully utilized. EHA

acting as the information-energy interfaced unit, is modeled in AMEsim. It receives real-time inputs for the target control surface deflection angle $\delta_{ref}$ and hinge moment $M_h$ ,and outputs the actuator displacement $\mathbf{X}_p$ and measured deflection angle $\delta$. The energy domain model is encapsulated as an Functional Mock-up Unit(FMU) and imported into MATLAB for bidirectional interaction with the information domain, ensuring synchronized real-time computation. The EHA serves both as an actuator in the closed-loop flight control system and as an electrical load in the power system. Notably, the platform supports concurrent simulation of multiple control surface EHAs, including their actuation dynamics and power flow interactions.

Through the flight environment configuration module and the engine speed input module, real-time flight missions were set. The power flow characteristics extract and analysis module obtains power flow data between EHAs and the electrical power grid. The real-time simulation platform can simulate different types of aircraft performing automatic flight missions that meet flight safety, and monitors the power coupling flow characteristics, such as voltage and current, between the EHAs and the electrical power grid in real time.

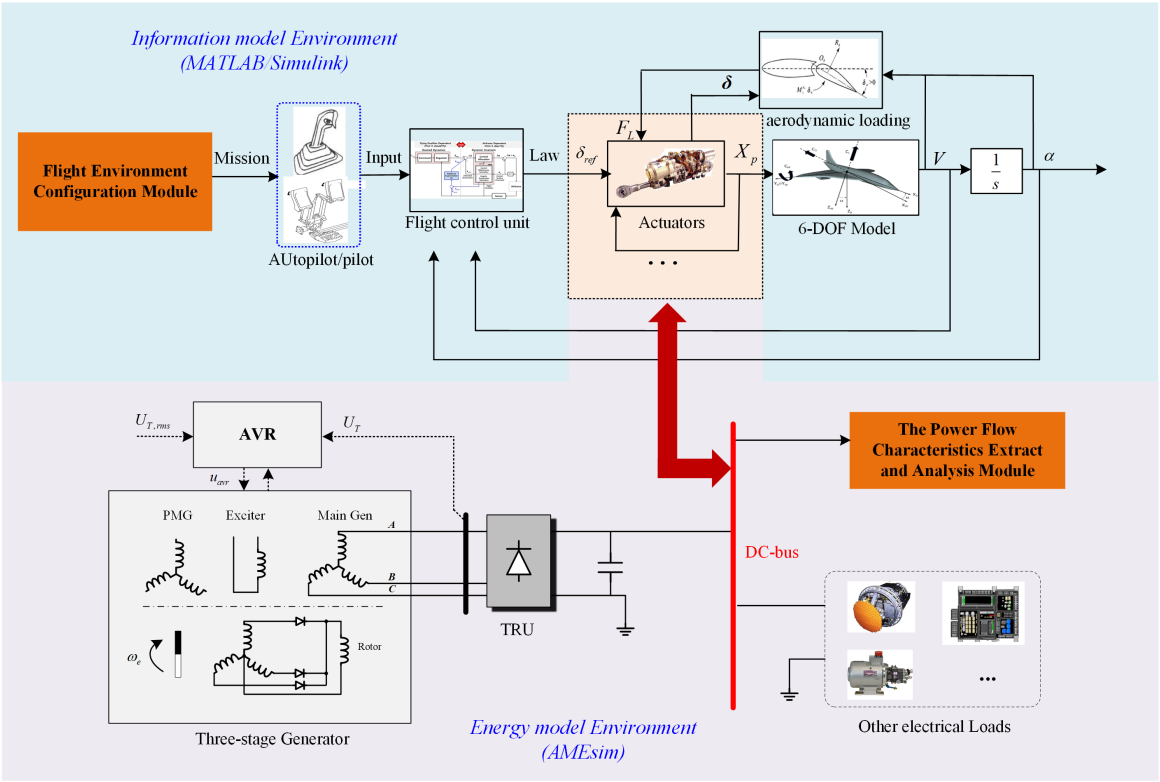



Figure 4 – Schematic diagram of the real-time simulation platform.

As illustrated in Figure 4, the autopilot generates reference commands by tracking deviations between the aircraft's current position and predefined trajectories. The flight control unit computes EHA commands based on errors between reference inputs and actual flight states. The EHA drives control surface deflections while calculating the 12-dimensional flight states Table 1 to determine the hinge moment. Port voltage and current fluctuations reflect power interactions between the EHAs and the electrical power grid. For simplicity, the navigation module's gain is set to 1, as this study focuses on flight state feedback rather than navigation performance.

## 3. Analysis

The analysis data presented in this paper is based on simulations of the F-16 model. The inertia data and wing geometric parameters for this model are shown in Table 2 and Table 3.

In this paper, a reference flight condition, applicable to most flight mission scenarios, is selected for the simulation. The flight state parameters were given by $x = [165, 2.29, 0, 0, 2.29, 0, 0, 0, 0, 0, 0, 1800]^{\mathrm{T}}$ which means the aircraft nose is directed north, the aircraft's center of mass is at an altitude of 1800m, with no side-slip, no roll, no yaw, no angular acceleration, and both pitch angle and angle of

Table 2 – F-16 inertia data [25]

| Item | Symbol | Value | Unit |
|---|---|---|---|
| Weight | $W$ | 9268.64 | kg |
| Moment of inertia about axis $x_b$ | $I_x$ | 12874.84 | kg·m² |
| Moment of inertia about axis $y_b$ | $I_y$ | 75673.361 | kg·m² |
| Moment of inertia about axis $z_b$ | $I_z$ | 85552.10 | kg·m² |
| Body-fixed angular rates $\mathbf{Ox_bz_b}$ | $I_{xz}$ | 1331.41 | kg·m² |

Table 3 – F-16 wing geometric parameters [25]

| Item | Symbol | Value | Unit |
|---|---|---|---|
| Wing Span | $b$ | 9.144 | m |
| Wing Area | $S$ | 91.44 | m² |
| Mean Aerodynamic Chord Length | $c$ | 3.450 | m |

attack are 2.29°, with an air-speed of 165 m/s at the initial time. The six-degree-of-freedom nonlinear motion equations of the aircraft were expanded around this reference point, and by combining the inherent configuration parameters of the F-16, a linearized state-space representation is obtained. The EHA parameters designed to meet the flight mission requirements are listed in Table 4.

Table 4 – The EHA parameters

| Variable Name | Symbol | Value | Unit |
|---|---|---|---|
| Piston Area | $A_a$ | 0.00282 | $m$ |
| Pump Displacement | $D_p$ | 2.5 | $mL/rev$ |
| System Pressure | $\Delta P_{\max}$ | 28 | $MPa$ |
| Rotational Inertia | $J$ | 0.0003 | $kgm$ |
| Friction Coefficient | $K_f$ | 0.0001 | $Nm/rev/\min$ |
| Hydraulic Cylinder Stroke | $X$ | ±25 | $mm$ |
| mass of the piston and rod | $m_t$ | 5 | $kg$ |
| Volume between pump and cylinder | $V_l$ | $10^{-6}$ | $m^3$ |

## 3.1 Power Spectral Analysis

Eight common flight maneuver scenarios, including dive maneuver, climb maneuver, serpentine maneuver, roll maneuver, loop, half-loop, high-altitude spiral, and high-speed yo-yo, were selected as basic flight mission scenarios [26]. The motion states and the primary flight control surfaces involved in each flight mission scenario are shown in Table 5.

Based on the real-time simulation platform shown in Figure 4, the flight mission scenarios were input into the autopilot to extract key flight state parameters. The dynamic power spectrum cluster of the EHA was obtained through simulation.

Figure 5 shows the dynamic power spectrum clusters for the left and right aileron, elevator, and rudder across the eight flight mission scenarios. From the figure, it is evident that the power peaks of each actuator differ greatly under different maneuver tasks. Furthermore, the power demands of the same actuator in different maneuvers were distributed unevenly in both the time-domain and frequency-domain.

To fully capture the key features of the power spectrum cluster of the EHA, this research proposes a time-frequency domain principal component analysis method for the power spectrum. Considering that the power spectrum contains signals with time-varying frequency components, variational mode decomposition (VMD) is first used to decompose the spectrum into the sum of several intrinsic mode power components. Then, the Hilbert transform is applied to each intrinsic mode power component to obtain its instantaneous frequency and amplitude, forming the principal component power spectrum cluster of the analyzed power spectrum.

Table 5 – Motion states and primary flight control surfaces in flight mis-sion scenarios

| Flight Mission Scenario | Motion State | Primary Flight Control Surface |
|---|---|---|
| Dive Maneuver | Pitch | Elevons |
| Climb Maneuver | Pitch | Elevons |
| Roll Maneuver | Roll, Yaw | Ailerons, Rudder |
| Serpentine Maneuver | Roll, Yaw | Ailerons, Rudder |
| High-altitude Spiral | Roll, Yaw | Ailerons, Rudder |
| Loop | Pitch, Roll, Yaw | Elevons, Ailerons, Rudder |
| Half-loop | Pitch, Roll, Yaw | Elevons, Ailerons, Rudder |
| High-speed Yo-yo | Pitch, Roll, Yaw | Elevons, Ailerons, Rudder |

In the VMD algorithm, the variational problem can be described as follows: under the constraint that the sum of all intrinsic mode power functions (IMPFs) equals the input power spectrum $P(t)$ , seek k intrinsic mode power components $P_k(t)$ that minimize the total estimated bandwidth of each component. The specific construction steps are as follows.
Using the Hilbert transform, the analytic signal of each intrinsic mode power component is obtained, and its single-sided spectrum is determined as follows:

$$\left(\delta(t)+\frac{j}{\pi t}\right)*P_k(t) \tag{30}$$

By adjusting the exponential term, the estimated cen-tral frequency of each intrinsic mode power component is modulated, and the spectrum of each component is shifted to the corresponding base frequency band:

$$\left[\left(\delta(t)+\frac{j}{\pi t}\right)*P_k(t)\right]e^{-j\omega_k t} \tag{31}$$

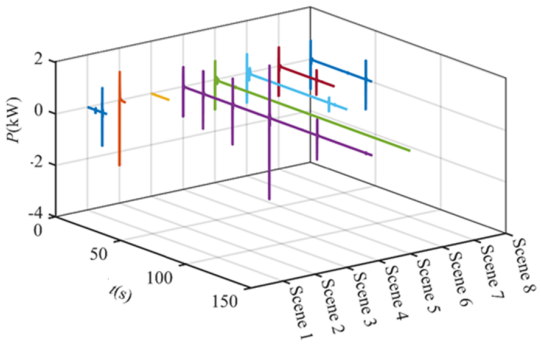
Through square $L^2$ regularization and Gaussian $H^1$ smoothing, the bandwidth of each IMPF component is estimated, with the total bandwidth of all IMPFs constrained to be minimized. The bandwidth of each IMPF is estimated by computing the squared norm of the gradient of the demodulated signal. Suppose the original power spectrum $P(t)$ is decomposed into k IMPF components, the corresponding constrained variational model is expressed as follows:

$$\begin{cases} \min\limits_{\{p_k,w_k\}}\left\{\sum\limits_k \partial_t\left\|\left[\left(\delta(t)+\frac{j}{\pi t}\right)*P_k(t)\right]e^{-jw_k t}\right\|_2^2\right\} \\ s.t.\sum\limits_k P_k = P(t) \end{cases} \tag{32}$$

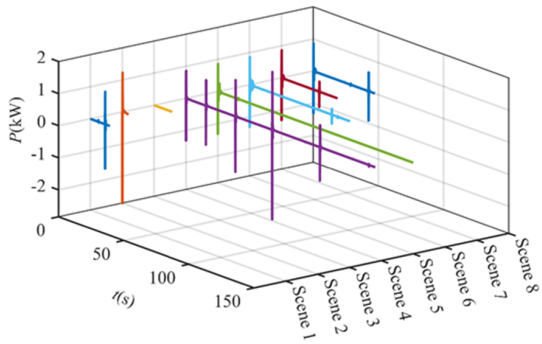
where $\{P_k\}=\{P_1,P_2,\cdots,P_k\}$ represents the k components obtained by VMD, and $\{\omega_k\}=\{\omega_1,\omega_2,\cdots,\omega_k\}$ denotes the frequency center of each IMPF component.
To obtain the optimal solution of the constrained variational model, a quadratic penalty factor $\alpha$ and a Lagrange multiplier $\lambda(t)$ are introduced, transforming the constrained variational problem into an unconstrained one. The quadratic penalty factor $\alpha$ ensures the accuracy of the reconstructed signal, while the La-grange multiplier $\lambda(t)$ strengthens the constraints. The extended Lagrange expression is given by:

$$L(\{P_k\},\{w_k\},\lambda)=\alpha\sum_k\left\|\partial_t\left[\left(\delta(t)+\frac{j}{\pi t}\right)*P_k(t)\right]e^{-jw_k t}\right\|_2^2+\left\|P(t)-\sum_k P_k(t)\right\|_2^2+\left\langle\lambda(t),x(t)-\sum_k P_k(t)\right\rangle \tag{33}$$

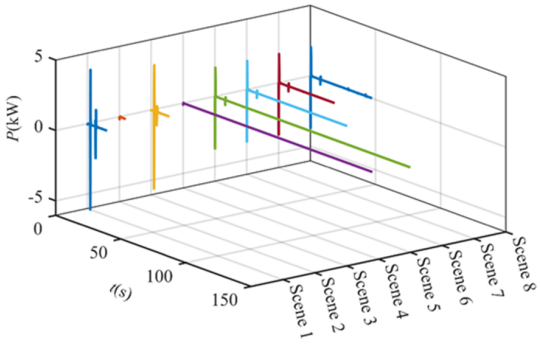
The VMD method uses the Alternating Direction Method of Multipliers (ADMM) to solve the above vari-ational problem by alternately updating $P_k^{n+1}$ , $\omega_k^{n+1}$ , and $\lambda^{n+1}$ , seeking the saddle point of the extended La-grange expression.
The initial update forms of $\{P_k\}$, $\{\omega_k\}$ , and $\lambda^k$ in ADMM are as follows:



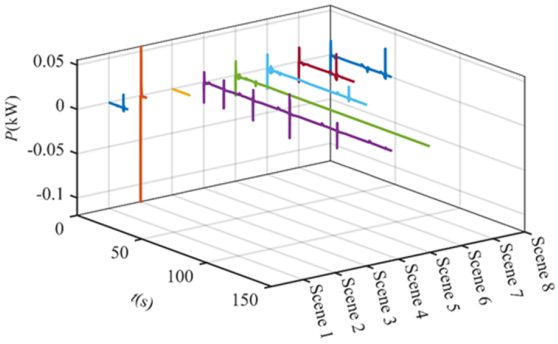

Dynamic power spectrum of Left aileron




Dynamic power spectrum of Right aileron




Dynamic power spectrum of Elevator




Dynamic power spectrum of Rudder

Figure 5 – The dynamic power spectrum clusters.

$$\begin{cases} P_k^{n+1} = \arg\min\limits_{u_k} \mathscr{L}\left(\left\{P_{i<k}^{n+1}\right\}, \left\{P_{i>k}^{n}\right\}, \left\{\omega_i^n\right\}, \lambda^n\right) \\ \omega_k^{n+1} = \arg\min\limits_{\omega_k} \mathscr{L}\left(\left\{P_i^{n+1}\right\}, \left\{\omega_{i<k}^{n+1}\right\}, \left\{\omega_{i\geq k}^{n}\right\}, \lambda^n\right) \\ \lambda^{n+1} = \lambda^n + \tau\left(P - \sum\limits_{k=1}^{K} p_k^{n+1}\right) \end{cases} \tag{34}$$

The solution to $P_k^{n+1}$ is formulated as follows:

$$P_k^{n+1} = \arg\min_{p_k \in P}\left\{\alpha\left\|\partial_t\left[\left(\delta(t)+\frac{j}{\pi t}\right) * P_k(t)\right] e^{-j\omega_k t}\right\|_2^2 + \left\|P(t) - \sum_i P_i\left(t+\frac{\lambda(t)}{2}\right)\right\|_2^2\right\} \tag{35}$$

where $\omega_k$ is equivalent to the Fourier transform of $\omega_k^{n+1}$ , and $\sum\limits_i P_i(t)$ corresponds to $\sum\limits_{i\neq k} P_i(t)^{n+1}$. By applying Parseval's and Pancheri's theorems, the above expression is transformed into the frequency domain:

$$\hat{P}_k^{n+1} = \arg\min_{p_k \in P}\left\{\alpha\left\|j\omega\left[(1+\operatorname{sgn}(\omega+\omega_k))\hat{P}_k(\omega+\omega_k)\right]\right\|_2^2 + \left\|\hat{P}(\omega) - \sum_i \hat{P}_i(\omega) + \frac{\hat{\lambda}(\omega)}{2}\right\|_2^2\right\} \tag{36}$$

Substitute $\omega$ with the variable $\omega - \omega_k$ :

$$\hat{P}_k^{n+1} = \arg\min_{p_k \in P}\left\{\alpha\left\|j(\omega-\omega_k)\left[(1+\operatorname{sgn}(\omega))\hat{P}_k(\omega)\right]\right\|_2^2 + \left\|\hat{P}(\omega) - \sum_i \hat{P}_i(\omega) + \frac{\hat{\lambda}(\omega)}{2}\right\|_2^2\right\} \tag{37}$$

This is then converted into the form of an integral over the non-negative frequency range:

$$\hat{P}_k^{n+1} = \arg\min_{p_k \in P} \left\{ \int_0^{\infty} 4\alpha(\omega-\omega_k)^2 \left|\hat{P}_k(\omega)\right|^2 + 2\left|\hat{P}(\omega) - \sum_i \hat{P}_i(\omega) + \frac{\hat{\lambda}(\omega)}{2}\right|^2 d\omega \right\} \tag{38}$$

At this point, the solution to the quadratic optimization problem is obtained as:

$$\hat{P}_k^{n+1}(\omega) = \frac{\hat{P}(\omega) - \sum_{i\neq k} \hat{P}_i(\omega) + \frac{\hat{\lambda}(\omega)}{2}}{1+2\alpha(\omega-\omega_k)^2} \tag{39}$$

Similarly, the frequency center update problem is transformed into the frequency domain:

$$\hat{u}_k^{n+1} = \arg\min_{\omega_k} \left\{ \int_0^{\infty} (\omega-\omega_k)^2 \left|\hat{P}_k(\omega)\right|^2 d\omega \right\} \tag{40}$$

The updated method for the frequency center is derived as:

$$\omega_k^{n+1} = \frac{\int_0^{\infty} \omega \left|\hat{P}_k(\omega)\right|^2 d\omega}{\int_0^{\infty} \left|\hat{P}_k(\omega)\right|^2 d\omega} \tag{41}$$

where $\hat{P}_k^{n+1}(\omega)$ corresponds to the current residual $\hat{P}(\omega) - \sum_{i\neq k} \hat{P}_i(\omega)$'s Wiener filtering; $\omega_k^{n+1}$ is the centroid of the power spectrum of the current intrinsic mode power component; and the real part of the inverse Fourier transform of $\{\hat{P}_k(\omega)\}$ is $\{\hat{P}_k(t)\}$ .

The dynamic power spectrum decomposition result for the left aileron during the serpentine maneuver, as shown in Figure 6 , includes the power spectrum decomposition of the left aileron and the frequency spectrum of the IMF components within the range of 0 to 15 Hz.

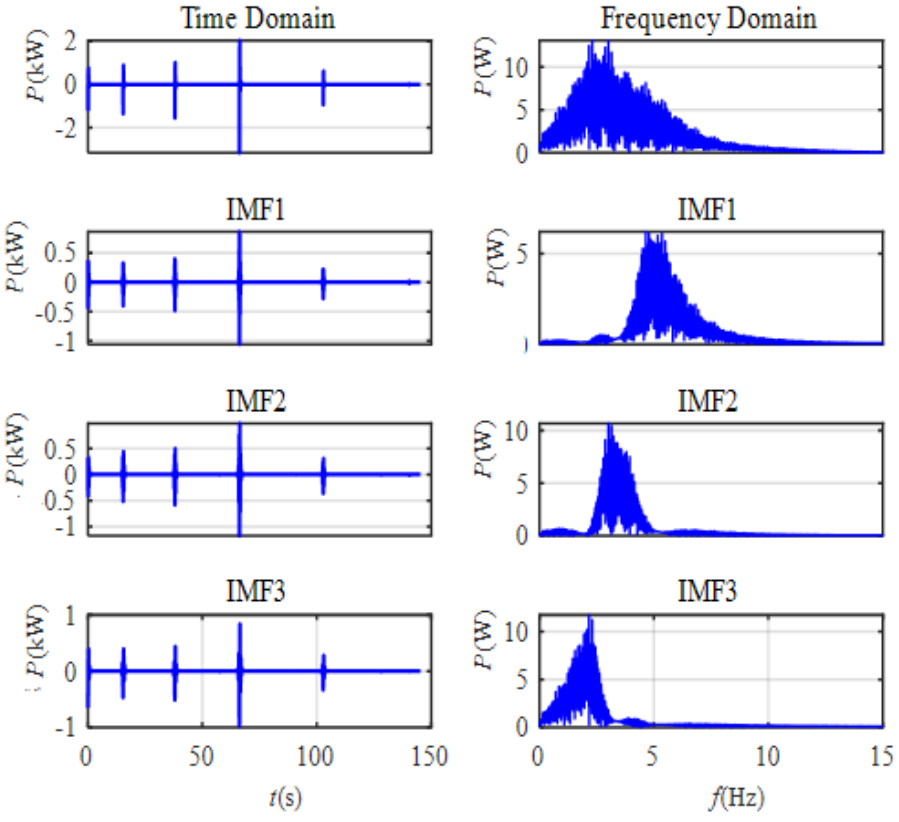



Figure 6 – The decomposition result of the power spectrum and the frequency spectrum of each IMPF component.

For a given IMPF $P_k(t)$, perform the Fourier transform:

$$P_k(\omega) = \int_T P_k(t)\, e^{-j\omega t} dt = \int_T P_k(t) \left[\cos(\omega t) - j\sin(\omega t)\right] dt \tag{42}$$

Multiply the power spectrum of the real signal by the step function shown in Equation 42, keeping the positive frequency part unchanged and eliminating the negative frequency part:

$$\varepsilon(\omega) = \begin{cases} 0, & \omega < 0 \\ 0.5, & \omega = 0 \\ 1, & \omega > 0 \end{cases} \quad or \varepsilon(\omega) = \frac{1}{2}(1 + \mathrm{sgn}(\omega)) \tag{43}$$

where the step function can be expressed as follows:

$$\mathrm{sgn}(\omega) = \begin{cases} 1, & \omega > 0 \\ 0, & \omega = 0 \\ -1, & \omega < 0 \end{cases} \tag{44}$$

The inverse Fourier transform of can be written as follows:

$$F^{-1}(\mathrm{sgn}(\omega)) = \frac{1}{2\pi} \lim_{a \to \infty} \left[ 0 - \left( \frac{1}{-a + jt} - \frac{1}{-a - jt} \right) \right] = \frac{1}{2\pi} \frac{-2}{jt} = \frac{j}{\pi t} \tag{45}$$

The single-sideband signal can be directly obtained in the time domain by convolution:

$$P_+(t) = P(t) * \left[ \delta(t) + \frac{j}{\pi t} \right] = P(t) + jP(t) * \frac{1}{\pi t} \tag{46}$$

The Hilbert transform of the power spectrum is defined as:

$$\hat{P}(t) = P(t) * \frac{1}{\pi t} = \frac{1}{\pi} \int_{-\infty}^{+\infty} \frac{P(\tau)}{t - \tau} d\tau \tag{47}$$

$$h(t) = \frac{1}{\pi t} \leftrightarrow h(\omega) = \begin{cases} -j = e^{-\frac{\pi}{2} j}, & \omega > 0 \\ 0, & \omega = 0 \\ j = e^{\frac{\pi}{2} j}, & \omega < 0 \end{cases} \tag{48}$$

For an intrinsic mode power component of the power spectrum obtained by variational mode decomposition, its conjugate signal is given by the Hilbert transform as:

$$\hat{P}_k(t) = a_k(t) \sin \phi_k(t) \tag{49}$$

The analytic signal formed by the original power spectrum is:

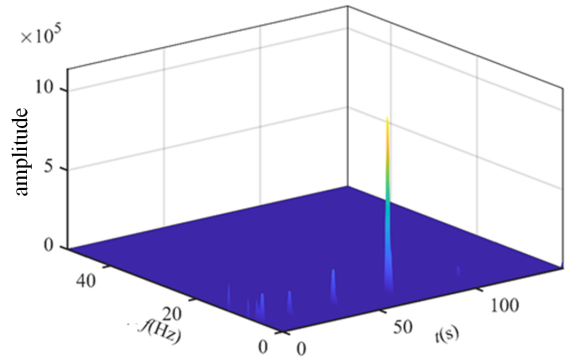
$$z_k(t) = P_k(t) + j\hat{P}_k(t) = A_k(t)\, e^{j\phi_k(t)} \tag{50}$$

where $\sqrt{A_k(t)}$ is the instantaneous amplitude of $P_k(t)$ , and $w_k(t) = \phi_k'(t)$ is the instantaneous frequency of $P_k(t)$ . By applying the Hilbert transform to each intrinsic mode power component, the instantaneous frequency and amplitude variation over time can be calculated, providing the Hilbert spectrum of each IMPF component, as shown in Figure 7 .

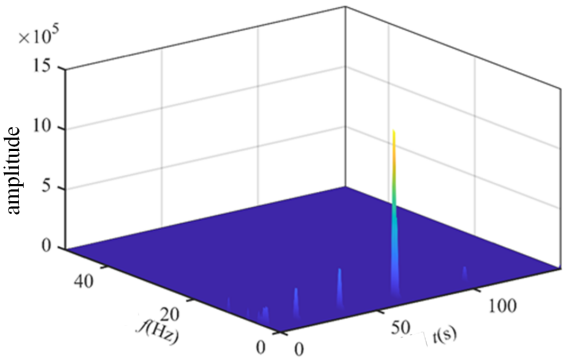
By integrating the Hilbert spectrum along the time axis, the relationship between amplitude, time, and frequency is transformed into a relationship between amplitude and frequency. This can be expressed as follows:

$$h(f) = \int_0^T H(t, f)\, dt \tag{51}$$

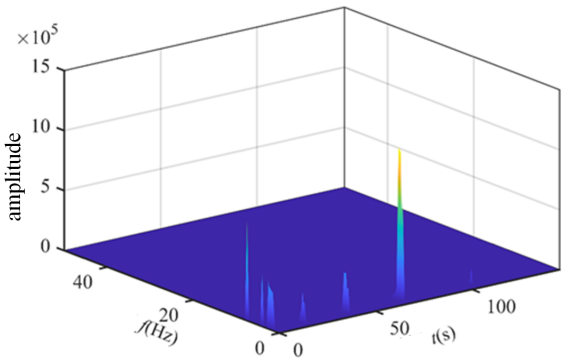
The marginal spectrum describes the distribution of amplitude across the frequency axis. The marginal spectrum of all IMF components of the original power spectrum in the 0-15 Hz range is shown, with a zoom-in of the 0-15 Hz range in Figure 8. From this, we can see that the main energy




(a) IMPF1




(b) IMPF2




(c) IMPF3

Figure 7 – Hilbert spectra of each IMPF component.

of the analyzed power spectrum is distributed at 1.91 Hz, 3.37 Hz, and 5.23 Hz. The corresponding power values at these frequencies can be obtained.

The main component power spectrum cluster of the left aileron during the serpentine maneuver is shown in Figure 8. The primary component power composition is shown in Table 6, which can be used in the EHA development process for load testing and guides the EHA design.

## 3.2 Power Flow Characteristic Analysis

### *3.2.1 Single-EHA–Grid Power-Flow Coupling Characteristics*

In order to validate the power flow characteristics between local EHA and the electrical power grid, clarify the dynamic mapping relationship between energy fluctuations and flight missions, and quantify the impact of the power flow on the electrical power grid, a simulation of the power flow characteristics of a single EHA during flight missions was conducted. Data was extracted and analyzed using the power flow characteristics extract and analysis module of the real-time simulation platform.

Figure 9,Figure 10,Figure 11illustrates the voltage and current curves of the EHA and the electrical

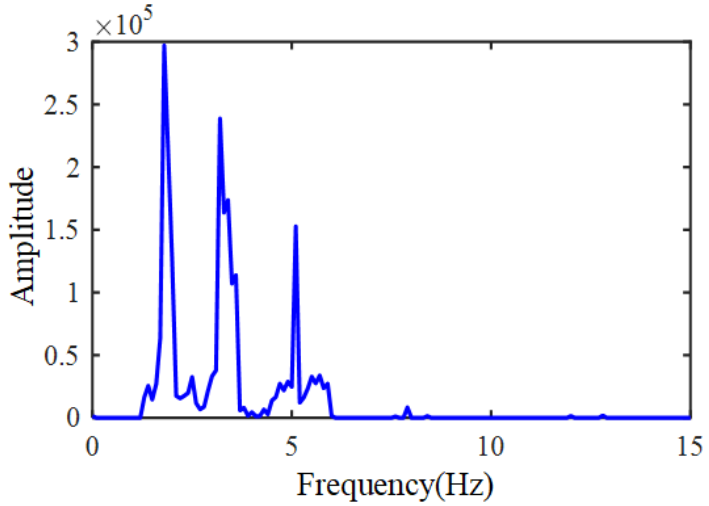



Figure 8 – Marginal spectrum of the power spectrum in 0–15 Hz.

Table 6 – Main component power spectrum cluster of left aileron in serpentine maneuver

| No. | Power(W) | Time(s) |
|---|---|---|
| 1 | $1186.26sin(2\pi 1.91t)$ | 145.33 |
| 2 | $1128.28sin(2\pi 3.37t)$ | 145.33 |
| 3 | $1025.06sin(2\pi 5.23t)$ | 145.33 |

grid port during dive, climb, and roll maneuvers.The simulation time for all cases is 15 seconds, with a solver step size of 0.001 seconds.

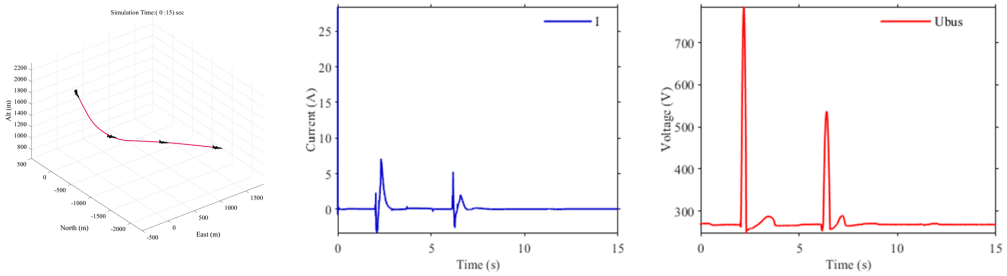
According to the current curves, the fluctuations in the actuator port current occur simultaneously with changes in the hinge moment and actuation command. This indicates that during the flight mission, changes in the operating conditions of the electric actuator, such as the hinge moment and displacement command of the control surface, induce energy fluctuations between the electric actuator and the electrical power grid of aircraft system.Furthermore, according to the voltage curves, it is observed that the bus voltage of the electric actuator port increases due to energy regeneration, which is consistent with theoretical analysis.

For the diving maneuver, the elevator EHA port voltage reaches 785.69 V, exceeding the 270 VDC nominal requirement specified in MIL-STD-704F [27] by 190.1%. For the climbing maneuver, the elevator EHA port voltage reaches 788.78 V, corresponding to a 192.14% exceedance of the 270 VDC requirement. In contrast, during the rolling maneuver, the EHA port voltage remains within the MIL-STD-704F allowable range of 250–280 VDC, indicating that the electrical grid operates in a stable and safe condition. These results demonstrate that the EHA–grid power-flow coupling characteristics are strongly mission dependent.

### *3.2.2 Multi-EHA–Grid Power-Flow Coupling Characteristics*

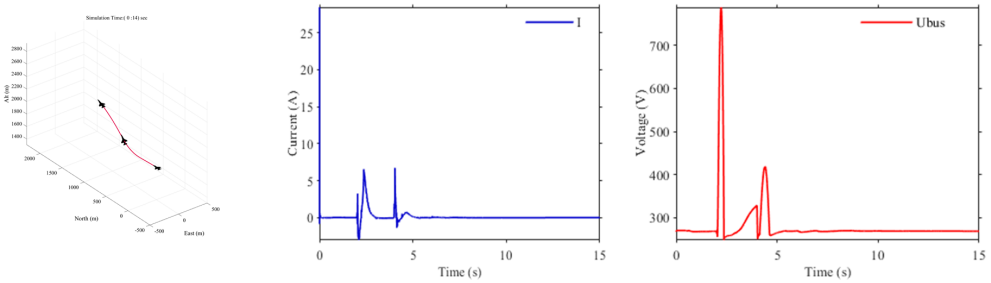
To more accurately reflect the real power flow characteristics between the EHAs and the power grid during aircraft maneuvers, and to explore the power coupling relationships between multiple actuators and the power grid, the cross-domain dynamic integrated model was simulated for four main flight control surface EHAs: the left aileron, right aileron, elevator, and rudder. Data was extracted and analyzed using the power flow characteristics extract and analysis module of the real-time simulation platform.

Figure 12 illustrates the voltage and current fluctuation curves of the four primary flight control surface EHAs and the power grid port during a dive maneuver. (a) shows the dive maneuver profile, (b) shows the port voltage; (c-1) shows the current at the left aileron EHA port; (c-2) shows the current at the right aileron EHA port; (c-3) shows the current at the elevator EHA port; (c-4) shows the current at the rudder EHA port. The simulation time is 15 seconds with a solver step size of 0.001 seconds.



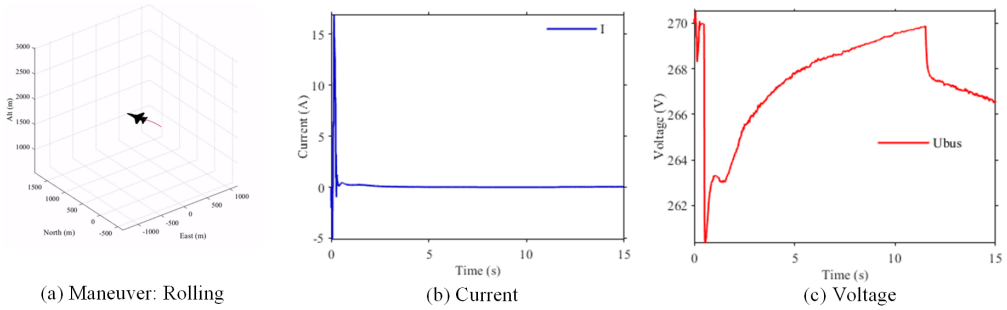

(a) Maneuver: Diving (b) Current (c) Voltage

Figure 9 – The voltage and current during dive maneuver.




(a) Maneuver: Climbing (b) Current (c) Voltage

Figure 10 – The voltage and current during climb maneuver.




(a) Maneuver: Rolling (b) Current (c) Voltage

Figure 11 – The voltage and current during roll maneuver.

As shown in the current curves of Figure 12 (c), the currents of the primary flight control EHAs exhibit dynamic fluctuations throughout the mission. Moreover, the currents of different actuators show both positive and negative values at the same time, indicating bidirectional power flow between the actuators.

Furthermore, based on the voltage and current curves in Figure 12 the voltage rising primarily occur during the energy feedback phases of the elevator EHA and aileron EHAs. This suggests that the elevator and ailerons have higher power demands during the dive maneuver, which aligns with the relationships of the primary flight control surfaces during a dive maneuver as summarized in Table 5. Similarly, the power flow characteristics of the other seven maneuver types also conform to their respective relationships, though they are not detailed here due to space limitations.

It is noteworthy that the comprehensive voltage fluctuation curve in Figure 12 exhibits three voltage peaks at 2.2s, 6.4s, and 11.3s, with peak values exceeding the MIL-STD-704F [27] voltage stability requirement for a 270 VDC power grid by 192.59%, 93.39%, and 61.34%, respectively. The total duration of voltage exceedance ac-counts for 8.09%, and the longest transient voltage duration is 0.23s. By comparing Figure 9(c) and Figure 12(b), it can be observed that Peak 1 is primarily driven by energy regeneration from the elevator EHA, while the aileron EHAs and rudder EHA simultaneously trigger higher voltage transients. Peaks 2 and 3 are dominated by energy injection from the aileron EHAs and rudder EHA. These observations indicate that the interaction between multiple

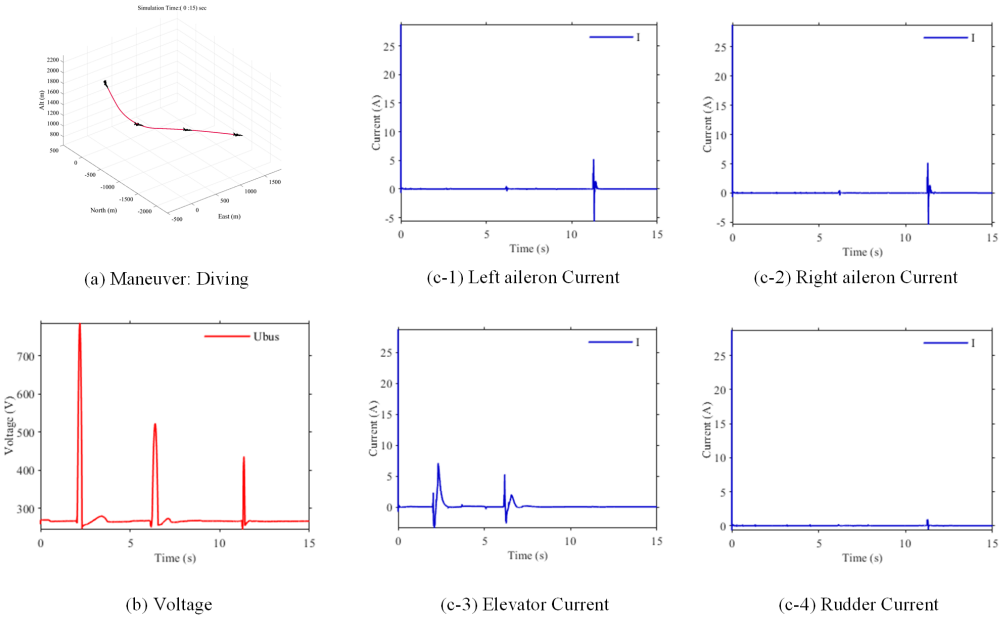



Figure 12 – Multi-EHA current and DC bus voltage during dive maneuver.

EHAs and the electrical grid presents comprehensive power-flow coupling characteristics, in which actuator-induced power flows are superposed or attenuated at different time instants.

## 4. Experimental Validation

To validate the accuracy of the cross-domain modeling and analysis approach, a test bench is designed to investigate the power flow characteristics between EHAs and the electrical power grid of aircraft system. As shown in Figure 13, the test bench consists of a DC power supply emulator, a real-time simulator, power diodes, filtering capacitors, two electronic loads, and an upper computer.

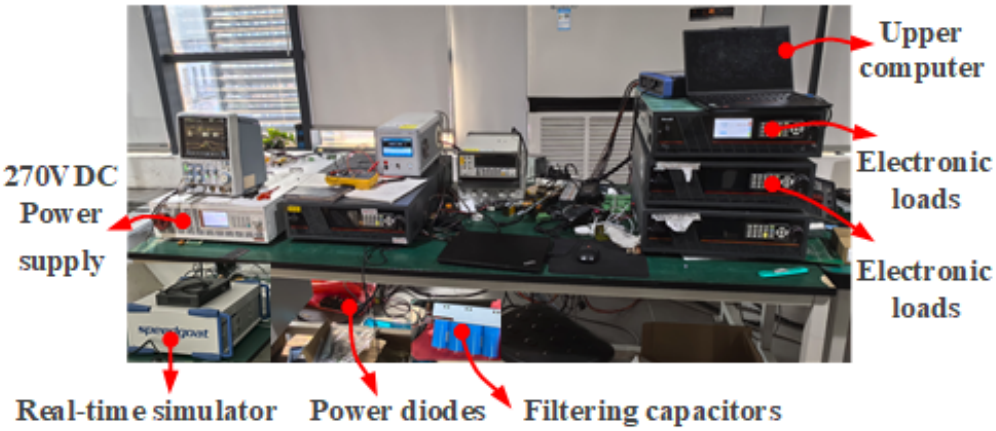



Figure 13 – Test bench for power flow characteristics.

The DC power supply emulator is used to emulate the aircraft three-stage generator and rectifier circuit, providing a 270VDC power output. Two electronic loads are employed to simulate two EHA units within the same flight control system. The real-time simulator executes the simulation program, which calculates the power demands from flight missions to actuator operations. It is important to note that the filtering capacitor at the rectifier output must be selected separately. Based on Equation 25, a 1680$mu$F, 1200 V withstand voltage film capacitor is selected. Additionally, a power diode is connected in series in the main DC power loop to simulate the restriction of power feedback in the power grid of aircraft system.

The experiment adopts hardware-in-the-loop (HIL). The DC power supply emulator operates in constant voltage mode, while the electronic loads operate in constant power mode. The real-time simu-

lator receives mission commands from the upper computer and transmits real-time EHA power state commands to the two DC electronic loads. Voltage and current data from the DC power supply and electronic loads are fed back to the simulator. The simulator's calculation cycle is set to 1 ms to ensure precise capture of dynamic power flow characteristics.

Test Case 1: Experimental validation of cross-domain dynamic model and the single-EHA–grid power-flow coupling characteristics

To validate the accuracy of the cross-domain dynamic model and single-EHA–grid power-flow coupling characteristics simulation results, tests were conducted for the following scenarios:

(1). EHA of elevator during a dive maneuver.
(2). EHA of elevator during a climb maneuver.
(3). EHA of Left aileron during a roll maneuver.

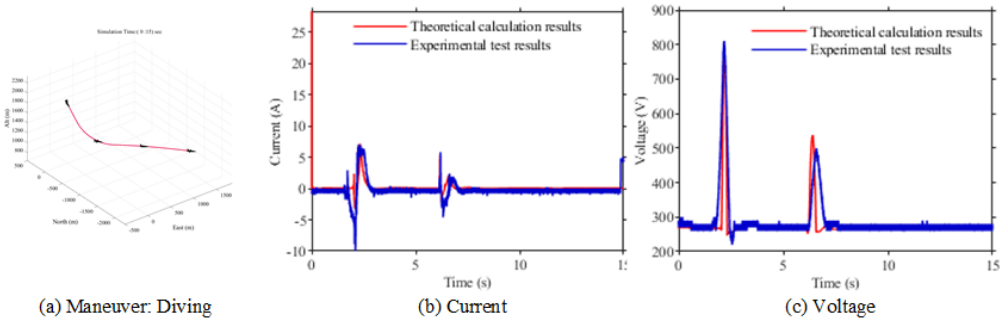



Figure 14 – Comparison of Experimental and simulation current/voltage under dive maneuver.

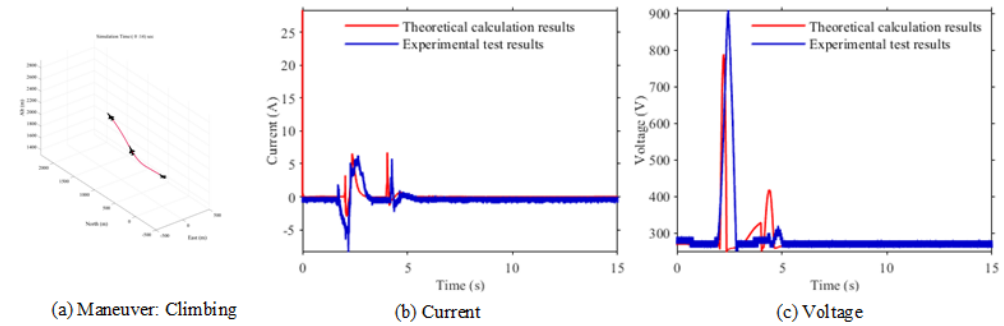



Figure 15 – Comparison of Experimental and simulation current/voltage under climb maneuver.

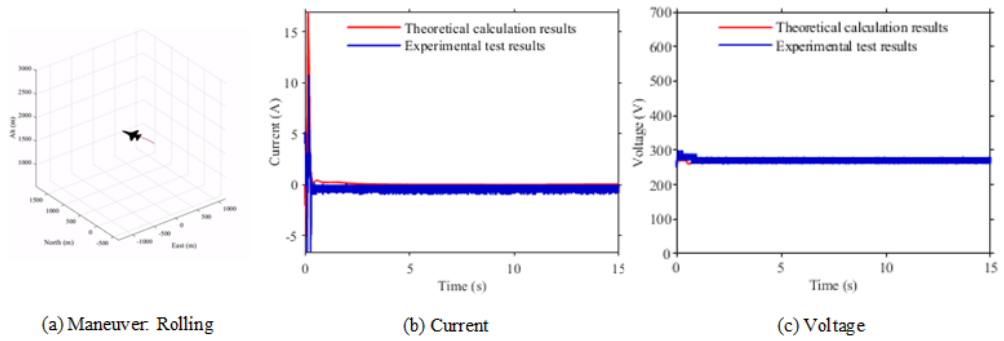



Figure 16 – Comparison of Experimental and simulation current/voltage under roll maneuver.

Figure 14, Figure 15,Figure 16 compare the experimental and simulation voltage and current at the electrical power grid ports. Due to the limited capability of the DC power supply to simulate the inductive reactive power and power factor within the generator of aircraft system, there are reasonable

discrepancies, such as lag and overshoot, between the experimental and simulation results. However, the experimental and theoretical voltage fluctuations of the EHA and power grid ports follow identical trends, with 92.4% consistency between measured results and simulation outputs. The close agreement between experimental and theoretical results validates the accuracy of the cross-domain dynamic model and the scientific rigor of the power flow analysis methodology, demonstrating the engineering value of this work.

Test Case 2: Experimental validation of multi-EHA–grid power-flow coupling characteristics

To investigate the power flow coupling characteristics between multiple EHAs and the electrical power grid of aircraft system, a "1-source, 2-loads" configuration was used to simulate cooperative operation scenarios:

(1). Dive: elevator EHA & left aileron EHA.

(2). Climb: elevator EHA & left aileron EHA.

(3). Roll: left aileron EHA & left aileron EHA.

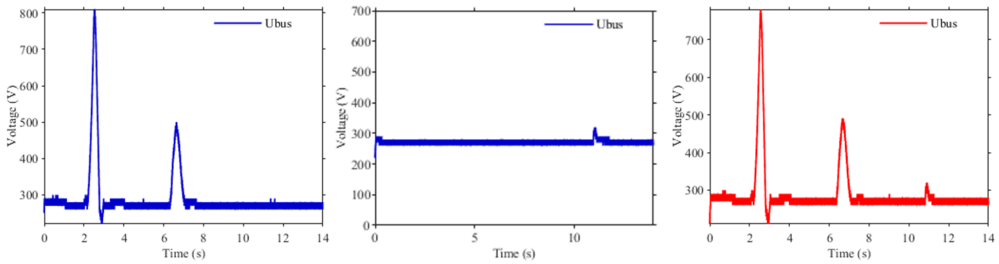



Figure 17 – Experimental voltage of and individual EHA and multiple EHAs under dive maneuver.

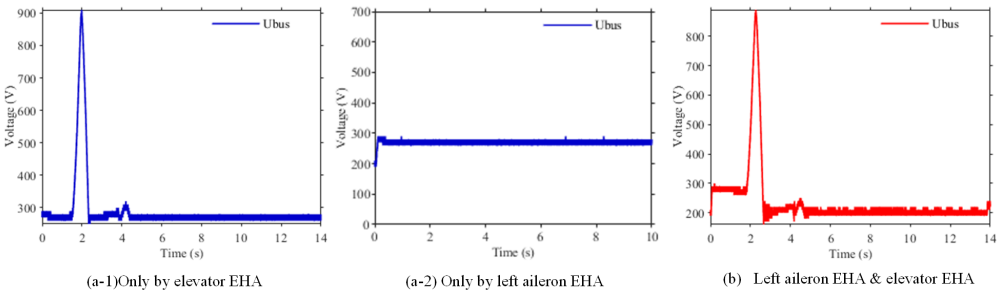



Figure 18 – Experimental voltage of and individual EHA and multiple EHAs under climb maneuver.

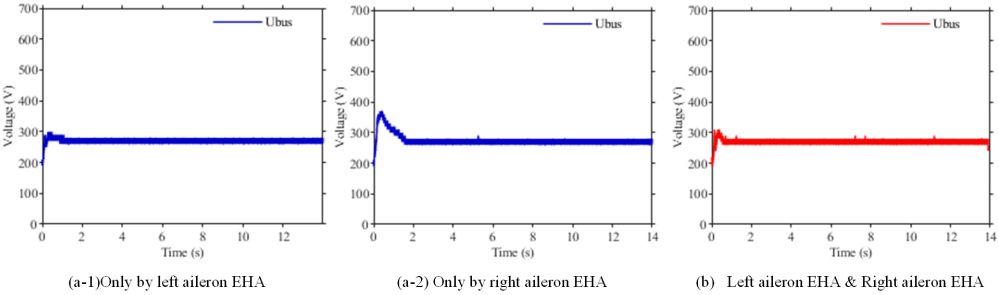



Figure 19 – Experimental voltage of and individual EHA and multiple EHAs under roll maneuver.

Figure 17, Figure 18, and Figure 19 illustrate the effects of single and multiple EHAs on electrical-grid voltage fluctuations under the same dive,climb,and roll flight mission. The results show that the DC-bus voltage fluctuation amplitude caused by multiple EHAs is not equal to the sum of the amplitudes caused by individual EHAs. This indicates that the multi-EHA–grid interaction cannot be evaluated by simply accumulating single-EHA responses. Instead, the overall grid voltage response is determined

by the temporal superposition, attenuation, and propagation of actuator-induced power flows, confirm the necessity of system-level multi-EHA power-flow coupling characterization.

## 5. Conclusion

This paper presents a comprehensive modeling and analysis approach for characterizing the power flow dynamics and coupling mechanisms of the flight control–actuation–electrical grid system in MEA. The main conclusions are summarized as follows.

1. A cross-domain integrated dynamic model of the flight control–actuation–electrical grid system is established.

The overall system is divided into the information domain and the energy domain, and the dynamic transfer relationships among flight control commands, actuator responses, and electrical power grid variations are jointly represented. A key cross-domain parameter identification method is proposed to quantitatively map information-domain variables to energy-domain variables. The developed model enables system-level characterization of the information transfer and energy interaction processes along the power-by-wire actuation chain. A real-time simulation platform is further constructed to implement and validate the proposed cross-domain integrated dynamic model.

2. A mission-oriented EHA power spectrum analysis method is proposed.

Based on the cross-domain integrated dynamic model, a time–frequency-domain principal-component power spectrum analysis method is developed to identify the dominant EHA power-demand spectra under different flight missions. The obtained spectra reveal the main frequency distribution characteristics of EHA actuation power demand and provide representative load profiles for EHA ground testing and design. This offers a model-based alternative for obtaining EHA electrical load characteristics without direct dependence on real flight tests.

3. Single- and multi-EHA power-flow coupling characteristics are analyzed and experimentally validated.

The simulated power-flow data are further used to characterize the coupling features between EHAs and the aircraft electrical power grid. For a single EHA, the local energy interaction characteristics between the EHA and the electrical power grid are analyzed. For multiple EHAs distributed across flight-control surfaces, the integrated power-flow coupling characteristics are investigated to reveal the superposition and propagation effects of actuator power demands within the electrical power system. A dedicated experimental platform is constructed to validate the identified single- and multi-EHA power-flow coupling characteristics, with the single-EHA–grid power-flow validation achieving a 92.4% agreement. The results confirm the effectiveness of the proposed model-based analysis framework.

Overall, the proposed approach provides a comprehensive model-based and analytical tool for mission-dependent EHA power-spectrum extraction, power-flow coupling characterization, and the design optimization of aircraft electrical power, actuation, and flight control systems in MEA.

## 6. Acknowledgements

This study was financially supported by the National Natural Science Foundation of China (No. 52272409), the National Key Laboratory of Aircraft Integrated Flight Control (JSY 6142219202403).

## 7. Contact Author Email Address

Yang Li:leeyoung303@buaa.edu.cn

## 8. Copyright Statement

The authors confirm that they, and/or their company or organization, hold copyright on all of the original material included in this paper. The authors also confirm that they have obtained permission, from the copyright holder of any third party material included in this paper, to publish it as part of their paper. The authors confirm that they give permission, or have obtained permission from the copyright holder of this paper, for the publication and distribution of this paper as part of the ICAS proceedings or as individual off-prints from the proceedings.

## References


[1] Raphael Felipe Gama Ribeiro, L. G. Trapp, and P. Lacava. Economical aspects of aircraft propulsion electrification. *2021 AIAA/IEEE Electric Aircraft Technologies Symposium (EATS)*, pages 1–18, 2021.

[2] Halime Hzarc and Uur Arifolu. Challenges with the electrification of aircraft for a sustainable and greener aviation. *International Journal of Sustainable Aviation*, 9(1):15, 2023.

[3] Alessandro Dell'Amico and Christopher Reichenwallner. A conceptual comparison of hydraulic and electric actuation systems for a generic fighter aircraft. *Aerospace (MDPI Publishing)*, 12(1), 2025.

[4] Jean-Charles MARÉ Wensen ZHANG, Jian FU. Investigations on mbse modelling and dynamic performance assessment of an electrical trimmable horizontal stabilizer actuator. *Chinese Journal of Aeronautics*, 36(11):417–433, 2023.

[5] R. Alden. C-141 and c-130 power-by-wire flight control systems. *IEEE*, 1991.

[6] Arthur E Sheridan and Robert Burnes. F-35 program history–from jast to ioc. In *2018 Aviation Technology, Integration, and Operations Conference*, page 3366, 2018.

[7] Yaoxing Shang, Xiaobin Li, Hao Qian, Shuai Wu, and Zongxia Jiao. A novel electro hydrostatic actuator system with energy recovery module for more electric aircraft. *IEEE Transactions on Industrial Electronics*, 67(4):2991–2999, 2020.

[8] R Navarro. Performance of an electro-hydrostatic actuator on the f-18 systems research aircraft. *16th Digital Avionics Systems Conference*, 1997.

[9] Tariq Mohd, Ali I. Maswood, Chandana J. Gajanayake, and Amit K. Gupta. Modeling and integration of a lithium-ion battery energy storage system with the more electric aircraft 270 v dc power distribution architecture. *IEEE Access*, pages 1–1, 2018.

[10] Hitoshi Oyori, Shingo Nakagawa, Hidefumi Saito, Norio Takahashi, and Noriko Morioka. System concept study of electrical management for onboard systems. *SAE Aerospace Systems and Technology Conference*, 2014.

[11] L. Barelli, G. Bidini, P. A. Ottaviano, F. Gallorini, and D. Pelosi. Coupling hybrid energy storage system to regenerative actuators in a more electric aircraft: Dynamic performance analysis and co2 emissions assessment concerning the italian regional aviation scenario. *Journal of Energy Storage*, page 45, 2022.

[12] Haoliang Yu, Tao Lei, Jiong Yang, Shuzhen Zhu, Xingyu Zhang, and Xiaobin Zhang. Design of cascaded hybrid energy storage system for airborne electro-hydraulic actuator loads. In *2024 IEEE 19th Conference on Industrial Electronics and Applications (ICIEA)*, pages 1–8. IEEE, 2024.

[13] Yanwu Xu and Zhuoran Zhang. Regenerated energy absorption methods for more electric aircraft starter/generator system. *IEEE Transactions on Power Electronics*, 38:7525–7534, 2023.

[14] Brian Stevens, Frank Lewis, and Eric N. Johnson. *Aircraft Control and Simulation: Dynamics, Controls Design, and Autonomous Systems, Third Edition*. Aircraft Control and Simulation: Dynamics, Controls Design, and Autonomous Systems, Third Edition, 2015.

[15] Michael V Cook. *Flight dynamics principles: a linear systems approach to aircraft stability and control*. Butterworth-Heinemann, 2012.

[16] Egbert Torenbeek. Airplane design, 1982.

[17] Haichun LIU, Yang LI, and Shaojun XIE. Aircraft rectifier with common ground of ac and dc power based on polarity conversion. *Acta Aeronautica et Astronautica Sinica*, 45(13):329539, 2024.

[18] Gaizka Martinez, Fermín Rodríguez, Ignacio Sanchez-Guardamino, Mikel Urnieta, and José Martín Echeverría. Improving the reliability of a future more electric aircraft dc power system through a novel topology and software combination. *International Journal of Electrical Power & Energy Systems*, 157:109795, 2024.

[19] Ajinkya Dnyaneshwar Yelore, S. Srinivasan, V. Rajaraman, S. Shamala, K Vasantha Kumari, and Dasari Venkayya. A novel feed-forward control scheme to meet transient response specifications of mil-std-704 for high-power aircraft generators. *IFAC-PapersOnLine*, 57:54–59, 2024.

[20] M. A. Zharkov, R. Y. Sarakhanova, and S. A. Kharitonov. New electric starter system based on on-board power network with hydrogen energy storage. *International journal of hydrogen energy*, (Oct.):85, 2024.

[21] I Jadric and D Borojevic. Modeling and control of a synchronous generator with an active dc load. *IEEE Transactions on Power Electronics*, 15(2):303–311, 2000.

[22] Y. Qiao, S. Wang, and J. Liu D. Tao M. Shi. Reliability model based on fault energy dissipation for mechatronic system. *Reliability engineering & system safety*, 250(Oct.):1.1–1.15, 2024.

[23] Junhui Zhang, LI Xuguang, LYU Fei, Felix Schlegel, Katharina Schmitz, LIU Shihao, Weidi Huang, and XU Bing. Critical operation range of electro-hydrostatic actuator pumps based on cylinder block tilting states. *Chinese Journal of Aeronautics*, page 103382, 2024.

[24] Shanxiao Du, Junjie Zhou, Jichao Hong, Huipeng Zhao, and Sanxi Ma. Application and progress of high-efficiency electro-hydrostatic actuator technology with energy recovery: A comprehensive review. *Energy Conversion and Management*, 321:119041, 2024.

[25] Mike C. Fox and Dana K. Forrest. Supersonic aerodynamic characteristics of an advanced f-16 derivative aircraft configuration. *NASA Langley Technical Report Server*, 1993.

[26] Zhifei Xi, Yingxin Kou, Zhanwu Li, Yue Lv, and You Li. An air combat maneuver pattern extraction based on time series segmentation and clustering analysis. *Defence Technology*, 36:149–162, 2024.

[27] Amrhein Marco, Raczkowski Brian, Pitel Grant, Wells Jason, Walters Eric, Lamm Peter, Iden Steven, Nairus John, Dewitt Laurence, and Hunnell Thomas. Standardized electrical power quality analysis in accordance with mil-std-704. *Sae International Journal of Aerospace*, 3(1):124–136, 2010.